A Sub-mm perspective on massive galaxies in the early universe

Schouws; S.T.M.

Chapter 1

Introduction

IN THE BEGINNING

The story of galaxy formation begins with the birth of the universe itself 13.8 billion years ago. At that moment the seeds for galaxy formation were planted as tiny quantum fluctuations.

Only 300 million years later, these tiny fluctuations had already grown into the first galaxies which are already surprisingly luminous and detectable by our most sensitive telescopes. Moreover, just another 400 million years later we observe galaxies that are chemically already quite similar to the galaxies we observe in the local universe today.

The aim of this thesis is to explore this early epoch of rapid galaxy formation from a sub-mm perspective, ranging from the detection of oxygen in one of the most distant galaxies currently known at $z > 14$ to a comprehensive study of the strikingly evolved galaxies we see at $z \sim 7$.

In this introduction we will briefly review the theoretical framework of galaxy formation, how we observe these galaxies in the early universe and finally the processes in the interstellar medium (ISM) driving emission in the far infrared (FIR) and the key observables of high redshift galaxies. We conclude with the main questions that this thesis attempts to address and give an overview of the results.

1.1 SETTING THE STAGE

This section broadly outlines the theoretical framework at the basis of galaxy formation, from the underlying cosmology to the linear collapse of dark matter halos. This part of galaxy formation is very well understood and analytically tractable and sets the stage on which galaxy formation takes place, with the complicated and messy physics of baryons that actually make up the galaxies we observe.

1.1.1 *The ΛCDM Universe*

Our current best description of the universe is the standard model of cosmology, known as the Lambda-Cold Dark Matter (ΛCDM) model. This framework has proven remarkably successful for understanding the origin and evolution of the universe. Within this model, the energy density of the present-day universe is dominated by two enigmatic components: dark energy ($\Omega_{\Lambda,0} \approx 0.7$) and cold dark matter ($\Omega_{\mathrm{DM},0} \approx 0.25$). The familiar baryonic matter that makes up gas, stars and planets only constitutes about 1/20 of the cosmic inventory ($\Omega_{\mathrm{baryon},0} \approx 0.05$) (Planck Collaboration et al. 2020).

For each component X, Ω_X is the ratio of its energy density, ρ_X, to the critical density, ρ_{crit}. The critical density is the natural density to compare to as it determines the shape of the universe. Current measurements agree that the sum of all components is unity ($\Omega = 1$), which implies that the universe does not have curvature.

These constituents, together with the assumption of isotropy and homogeneity, determine the expansion history of the universe. This expansion history is captured in the Friedmann equations, which are derived from the Einstein field equations for the Friedmann-Lemaître-Robertson-Walker metric. Solving the Friedmann equation gives the scale factor $a(t)$ as a function of time. The scale factor can be interpreted as the ratio between the size of the universe at time t relative to its present size. It furthermore is related to redshift as $a = 1/(1+z)$ and can thus be directly be inferred through spectroscopy by measuring z. Interestingly, this implies that at $z = 1$ the universe was only half the size of the current universe and at $z = 14$ the universe was much more compact at only $\sim$7% of its current size.

Because the energy density of each of the components in the universe scales differently with the scale factor, cosmic history can be divided into different epochs in which different components were dominant. In the current universe, dark energy became dominant around $z = 0.7$. Before the current epoch, the universe was matter dominated until very early in the universe ($z > 3400$), when radiation was the principal component. This means that most of cosmic structure formation and galaxy evolution took place in the matter dominated epoch.

1.1.2 *Collapse of Haloes*

The previous section described the evolution of a perfectly homogeneous and isotropic universe. However, the observed universe is filled with a rich hierarchy of structure. As mentioned before, these structures are the result of tiny fluctuations, set by the primordial power spectrum. Over long enough time these tiny fluctuations collapsed and formed the structures we observe today.

This collapse is governed by the interplay between self-gravity of these fluctuations, which seeks to amplify them, and the overall cosmic expansion, which works to dilute them ("Hubble friction"). The strength of a fluctuation is generally quantified in terms of the density contrast, $\delta(\mathbf{x}, t) = \frac{\rho(\mathbf{x},t) - \bar{\rho}(t)}{\bar{\rho}(t)}$, which measures the fractional overdensity at a given point in space relative to the cosmic mean density, $\bar{\rho}(t)$ at time t and location $\mathbf{x}$.

Conveniently, in the regime of tiny fluctuations ($\delta \ll 1$), the evolution of the overdensity can be calculated analytically. In a static universe, the collapse would be exponential, however in our expanding universe the collapse is generally power-law shaped. The precise rate of the growth depends critically on the dominant component of the universe's energy density at any given time. Specifically, during the matter dominated epoch, which is the epoch relevant for galaxy formation, structures grew as $\delta \propto (1+z)^{-1}$.

As fluctuations become more overdense, their evolution enters a highly non-linear phase. The gravitational collapse becomes a complex, multi-stream process that is analytically intractable, so numerical methods become necessary, such as cosmological N-body simulations.

Although linear theory cannot describe the nonlinear collapse itself, the spherical-collapse model establishes a useful correspondence between collapse and the linearly extrapolated density contrast. In this model, a perturbation is considered to have collapsed once its linearly extrapolated overdensity reaches the critical value $\delta_{lin,c} = 1.686$ (e.g. Gunn & Gott 1972; Press & Schechter 1974). This value does not represent the true overdensity of the perturbation, but rather it is the value that linear theory would predict at the time when the spherical perturbation formally collapses. By that stage the perturbation is already highly nonlinear and the process of virialization is underway.

1.1.3 *The Halo Mass Function*

The description of how fluctuations grow over time, cross $\delta_{lin,c}$ and collapse, can be combined with the initial distribution of the fluctuations as given by the primordial power spectrum. This gives an accounting of the number of collapsed halos of a certain mass in a fixed (comoving) volume at any point in time. The resulting distribution is known as the halo mass function (HMF).

The Halo Mass Function is shown in Figure 1.1 and exhibits a characteristic shape: a power-law at the low-mass end with a sharp exponential cutoff at the high-mass end. The sharp exponential cutoff is driven by the increasing rarity of massive haloes, which require a high sigma fluctuation in the primordial density field to be able to collapse early. In a fixed volume, there are not many such high-sigma fluctuations, causing the exponential cutoff. At the low mass end, the variance of the density contrast is much larger and crossing $\delta_{lin,c}$ is not a rare event. The power-law shape of this part of the HMF is predominantly driven by the shape of the primordial power spectrum.

For reference, in Figure 1.1 we show the number of halos that would be expected in a fixed survey volume of $1{\times}1$ deg^2 field of view, which is roughly typical for deep extragalactic surveys. Strikingly, this reveals a notable discrepancy between the predicted halo distribution and the galaxy populations we actually observe.

If we compare the number of galaxies spectroscopically confirmed at $z = 14$ and $z = 12$, the counts are roughly similar ($\sim 5 - 10$) (e.g. Harikane et al. 2023; Carniani et al. 2024). However, from the figure it is clear that for a given halo mass the expected number of halos increases by approximately an order of magnitude between z=14 and z=12. If galaxies simply traced the underlying halo population, we would expect a similar dramatic increase in galaxy counts, which is not supported by observations.

This discrepancy introduces what has been widely discussed in the literature as the "early galaxy tension" or the "early galaxy crisis" following the launch of the James Webb Space Telescope (JWST). Standard galaxy formation models, calibrated to match the galaxies we observe at lower redshifts, predicted a rapid, exponential decline in the UV luminosity function of galaxies at z>10. Instead, JWST has uncovered a surprisingly abundant population of exceptionally luminous, spatially extended, and chemically enriched systems.

The complicated connection between the underlying population of haloes and the galaxies we observe becomes even more apparent in the right panel of Figure 1.1. This figure shows the galaxy stellar mass function (GSMF) at $z = 7$ together with the HMF under the assumption that different fractions of the available baryons in each halo are converted to stars, i.e. a fixed star formation efficiency. Interestingly, there does not seem to be a fixed star formation efficiency that can explain the stellar masses we observe in galaxies across the full mass range and a mass-dependent efficiency is necessary to explain the data.

Both examples illustrate the stark differences between the predicted abundance of dark matter halos derived from beautiful analytic theory, and the complex real world of actual observed galaxy populations. Indeed, explaining both requires mechanisms that depend on (halo) mass and cosmic time. This is where baryonic processes take over, governing

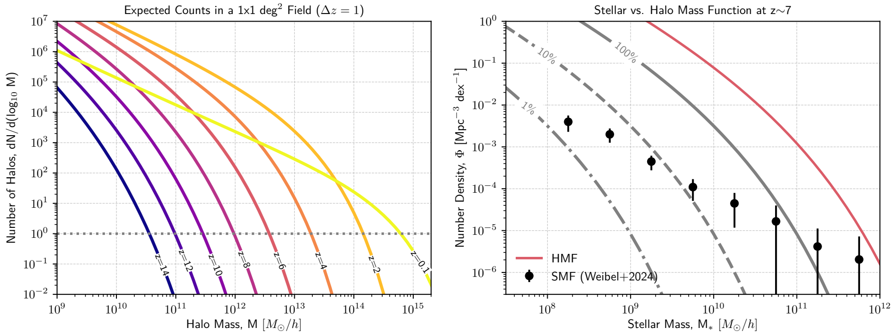

Figure 1.1. *Left panel:* The evolution of the dark matter halo mass function from $z = 14$ to $z = 0.1$. Instead of the usual counts per unit comoving volume it is shown in terms of number of halos per decade of mass in a $1{\times}1$ deg^2 field in a redshift interval of $\Delta z = 1$. The horizontal dashed line at y=1 indicates the threshold for expecting at least one halo per mass decade in such an area. *Right panel:* The halo mass function compared with the observed galaxy stellar mass function (GSMF) at $z = 7$ (Weibel et al. 2024). The grey lines illustrate the predicted GSMF under the simple assumption that a fixed fraction of the available baryons in every halo is converted into stars.

how gas cools and how different components of galaxies interact with this gas through feedback processes. How exactly these processes work is the most important open question in galaxy formation and evolution, and will be the focus of the next sections.

1.2 FROM DARK MATTER HALO TO GALAXY

The transformation of baryons within a dark-matter halo into an observable galaxy involves processes central to galaxy formation and evolution. Practically, to form a galaxy in a dark matter halo, large amounts of gas must undergo runaway collapse and form stars. This results in a competition between the self-gravity of the gas and its internal pressure. For gravity to win and form the stars we observe, the internal pressure must be sufficiently low and therefore the gas must become dense and cold.

However, there is a complication. As gas falls into the potential wells set by the dark matter, it converts potential energy into kinetic energy and is heated significantly. At high redshift, however, gas accretion is generally dominated by "cold mode accretion", where gas from the cosmic web flows directly into a developing galaxy along narrow, high-density filaments rather than spreading out into a spherical halo (Dekel et al. 2009). This bypasses the formation of a stable, hot atmosphere of gas enveloping the halo commonly found around massive halos at lower redshift. The inflowing gas is still heated to the halo's virial temperature, typically tens of thousands of Kelvin, through shocks where these streams converge at the halo's center. This high temperature causes the gas pressure to be far too high to allow the runaway gravitational collapse required to form stars. It is therefore crucial to cool the gas by radiating away this thermal energy.

1.2.1 *The Cooling Function*

This cooling is achieved when particles in the gas interact and convert their kinetic energy into radiation, which subsequently escapes and carries away thermal energy. There are several types of interactions that contribute to this and these processes depend on both temperature and the chemical composition of the gas. The combined efficiency of all processes is captured by the cooling function, denoted as $\Lambda(T, Z)$[1]. The cooling function for different metallicities is shown in Figure 1.2.

From the figure, two things can be noted. First, the presence of metals significantly enhances the ability of gas to cool. This is because metals open up numerous transitions in addition to those from hydrogen to radiate away energy. Second, there is a rapid drop in the cooling function below $\sim 10^4$ K. This is because at this temperature the hydrogen cooling channel shuts off catastrophically, both due to a lack of free electrons and insufficient thermal energy to excite hydrogen's lowest energy level (10.2 eV). Because hydrogen is the dominant component of any gas, the cooling rate drops by $>$4 orders of magnitude.

The precipitous drop in the cooling function creates a critical bottleneck, as gas would be unable to cool further were it not for mechanisms other than atomic hydrogen. This is where fine-structure line cooling and molecular cooling become paramount. Heavy elements like carbon and oxygen possess low-lying fine-structure energy levels that can be excited by collisions even in gas with temperatures of just a few hundred Kelvin. The same applies to molecules, which have rotational and vibrational excitations that can be excited at low temperatures.

Radiative de-excitation from these levels, producing far-infrared photons from lines such as [CII]158μm, allows the gas to bypass the 10.000 K

[1] It should be noted that the total cooling rate per unit of volume ($\mathcal{C}$) also strongly depends on the density $\mathcal{C} = n_e n_i \Lambda(T, Z)$, where n_e and n_i are the number densities of electrons and ions, respectively. This is because the radiative processes are two-body interactions involving an electron and an ion.

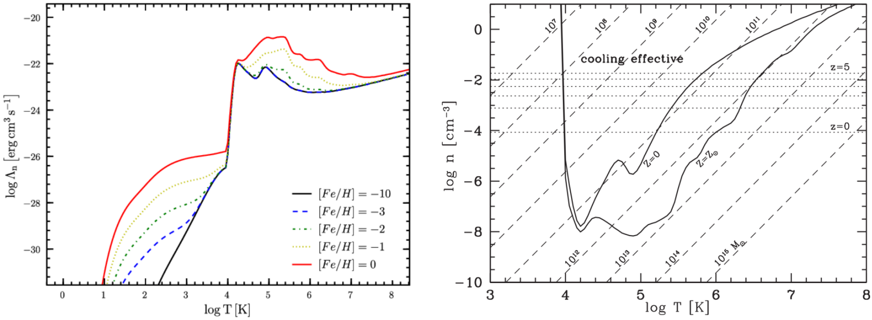

Figure 1.2. *Left panel:* The cooling function versus temperature for gas of different metallicities ([Fe/H]). Note the sharp increase in cooling above 10^4K and the strong dependence on metallicity. (Adapted from: Revaz et al. 2009) *Right panel:* The critical boundary for effective cooling ($t_{\rm cool} = t_{\rm ff}$) in the density-temperature plane for primordial and solar metallicity gas. Above this boundary cooling is effective, enabling catastrophic collapse. The dashed diagonal lines correspond to constant gas mass. The horizontal dotted lines indicate the characteristic density of virialized halos ($200\times\rho_{\rm crit}$). Because halos at higher redshift are intrinsically denser, gas within them is more likely to be in the effective cooling regime. For example, a gas mass of 10^8 $M_\odot$ resides in the inefficient region at z=0 but can cool effectively at z=5. (Adapted from: Mo et al. 2010)

temperature floor and continue its collapse. In the absence of metals, the only significant coolant below 10.000 K is molecular hydrogen (H_2), which is fragile and easily destroyed by UV radiation. The presence of metals therefore provides a far more robust and efficient cooling pathway in the low-temperature regime with cooling rates orders of magnitude higher than for primordial gas. These fine-structure cooling lines are at the core of the work presented in this thesis.

1.2.2 *Cooling Effectiveness*

To understand whether gas can collapse to form stars, we must compare two critical timescales: the cooling time ($t_{\rm cool}$) and the free-fall time ($t_{\rm ff}$).

The cooling time is the timescale over which the gas can radiate away its internal thermal energy (in the absence of heating), and it is defined as the ratio of the gas's thermal energy density to its cooling rate per unit volume. The cooling time scales as $t_{\rm cool} \propto T/n$. Notably, the cooling time decreases with increasing density. In contrast, the free-fall time represents the characteristic timescale for a cloud to collapse under its own gravity, which scales as $t_{\rm ff} \propto n^{-1/2}$ (e.g. Mo et al. 2010).

Cooling is considered "effective" when the cooling time is shorter than the free-fall time ($t_{\rm cool} < t_{\rm ff}$). In this regime, the gas loses its pressure support faster than it can dynamically respond to the change. This triggers a runaway process known as catastrophic cooling: as the gas cools and loses pressure, it gets compressed by gravity. Its density increases, which in turn shortens both the cooling time and the free-fall time, accelerating the collapse until stars are formed. The redshift of the universe plays a critical role here. The characteristic density of a virialized halo is tied to the critical density of the universe at that epoch, which scales as $(1 + z)^3$. Halos at high redshift are therefore intrinsically much denser, which dramatically shortens their free-fall times and makes the condition for effective cooling much easier to satisfy.

Figure 1.2 provides a powerful visualization of this concept, plotting gas density against temperature. The solid lines delineate the critical boundary where $t_{\rm cool} = t_{\rm ff}$ for both primordial (Z=0) and solar-metallicity gas (Z=$Z_\odot$). The region to the upper-left of these lines is where cooling is effective. The dashed diagonal lines show the virial temperature and density for halos of a given mass. The figure shows that at high redshifts, virtually all halos massive enough to form stars reside in this catastrophic cooling regime.

This leads to an interesting and well-known issue: the "overcooling problem" (Benson et al. 2003). A naive interpretation of the physics above predicts that nearly all the baryonic gas accreted onto dark matter halos should have cooled, collapsed, and been converted into stars long ago. However, observations reveal a starkly different picture, where only a small fraction of the available baryons in a typical halo have actually formed stars. This discrepancy implies that heating and momentum injection must counteract cooling and regulate collapse. These processes are collectively known as feedback.

1.2.3 *Feedback Processes and the Need for Numerical methods*

Feedback processes inject the energy and momentum into the ISM that is necessary to regulate the formation of stars to match the galaxies we observe. These processes can either enhance star formation (positive feedback) or suppress it (negative feedback).

Observations indicate that the integrated efficiency with which halos convert their available baryons into stars varies strongly with halo mass (e.g. right panel of Figure 1.1). In the local universe this is most clearly observed in the relation between the halo mass and stellar mass of galaxies. This efficiency peaks at a halo mass of approximately $10^{12}\,M_\odot$ and decreases toward both higher and lower masses. (e.g. Moster et al. 2013). Different feedback mechanisms are generally invoked to explain the declining efficiencies below and above this characteristic halo mass.

Unfortunately, these processes are highly nonlinear and have complex interactions between themselves. This makes the problem too complex to solve analytically and numerical models are necessary. Two principal modeling approaches are used: semi-analytic models (SAMs) and cosmological hydrodynamical simulations.

Semi-analytical models are built on dark-matter-only simulations. These dark-matter simulations provide the underlying foundation of dark matter haloes and how they evolve. The baryonic physics is then implemented using different "recipes" that describe the gas cooling, star formation, chemical enrichment and feedback processes. This is computationally very efficient, but generally provides limited spatial information and significantly simplifies all the complex processes happening in a galaxy.

In contrast, (Cosmological) hydrodynamical simulations directly solve the equations of gravity, hydrodynamics, and thermodynamics on Eulerian grids, moving mesh methods or using Lagrangian particle methods (e.g., Smoothed Particle Hydrodynamics or moving-mesh codes). Modern suites such as IllustrisTNG and EAGLE (Vogelsberger et al. 2014; Schaye et al. 2015) allow for a much more detailed look at the processes happening inside galaxies.

However, because the physical scales of the relevant processes that impact star formation are separated by orders of magnitude, both approaches ultimately rely on assumptions and "subgrid" recipes that determine how they model the formation and evolution of galaxies. Moreover, these recipes need to be calibrated on observed data and cannot be derived from first principles.

Currently, most models implement two primary modes of feedback[2]. The first mode is driven by stellar sources, both stellar winds and radiation from massive stars, but most importantly energy injected by supernova explosions. Stellar feedback is especially influential in low-mass halos because, in sufficiently low-mass systems, the energy released by even a small num-

[2] This is in addition to feedback driven by environment (e.g. ram-pressure stripping and strangulation) and galaxy-galaxy interactions.

ber of supernovae can become comparable to the binding energy of the interstellar gas (e.g. Mo et al. 2010).

For massive haloes, however, supernova feedback is insufficient to prevent overcooling and it is expected that a different mechanism becomes dominant. This second mode of feedback is driven by Active Galactic Nuclei (AGN), which are fueled by the accretion of gas onto the Super Massive Black Holes (SMBHs) that are expected to be in the nucleus of every galaxy. The infall of gas onto an SMBH converts a substantial fraction of the accreted rest-mass energy into radiation, winds, and jets, which can happen in either short-lived extreme bursts (quasar mode) or a slower sustained mode (radio-mode).

However, both for supernova feedback and AGN feedback, the exact way in which they couple to the gas and drive the feedback is still unknown and remains one of the major open questions in galaxy formation. This is where simulations provide useful guidance, as each simulation implements these feedback mechanisms and other subgrid physics in unique ways and they can subsequently be compared to observations across cosmic history. Testing these models requires observational constraints on gas density, temperature, ionization, and chemical enrichment, many of which are obtained through spectroscopy of the high-redshift ISM.

1.3 PROBING THE ISM AT HIGH REDSHIFTS

1.3.1 *Emission Lines as tracers of the ISM*

To understand which mechanisms are responsible for this critical regulation of star formation, it is essential to characterize the physical conditions in the ISM of galaxies. This perspective is enabled through the study of emission lines.

The conditions in the ISM, such as chemical abundance, temperature, density and properties of the ionizing spectrum drive the strength of different emission lines and the continuum. Therefore, by measuring and comparing the strength of emission lines and the continuum, and testing these against models for the ISM, it is possible to gain critical insights into the physical conditions inside galaxies.

In the FIR, there is a large variety of detectable emission lines originating from all phases of the ISM that are relevant for star formation, as illustrated in Figure 1.3. This can be complemented with strong emission lines from the rest-frame UV and optical parts of the spectrum. However, because of the higher energies of optical and rest-UV photons, these

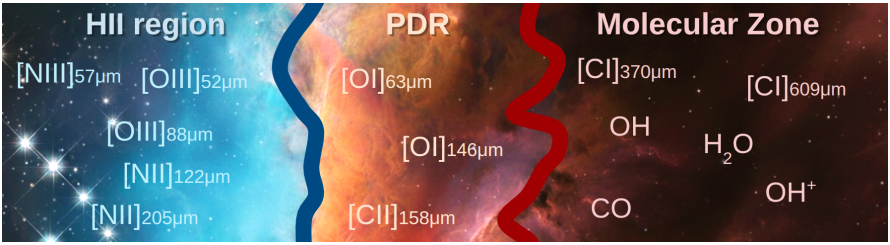

Figure 1.3. A schematic overview of some of the strongest emission lines available in the far-infrared. All phases of the ISM surrounding a star-forming region can be studied with several emission lines. These lines enable a unique view of the physical processes that dominate these regions.

lines predominantly originate from the hottest phases of the ISM ($\gtrsim$10.000 K). Therefore, in normal galaxies, optical and UV lines mostly originate from HII regions, which means that FIR lines offer a unique perspective on other colder/neutral phases of the ISM such as PDR regions and molecular clouds.

This thesis is focused on two of the strongest FIR lines that we can detect with current facilities, the [CII]158μm line and the [OIII]88μm. In the next sections, we will explore the physics governing these lines as well as the underlying dust continuum.

1.3.2 *The [CII]158μm line*

1.3.2.1 *Where does [CII] originate in the ISM?*

Due to its low ionization potential compared to hydrogen (11.3 eV versus 13.6 eV) and low critical density ($n_e \sim 10 - 45$ cm^{-3} at 100K and 8000K respectively (e.g. Goldsmith et al. 2012)), [CII] can be emitted from all major phases of the ISM. In particular the ionized phase (HII regions and diffuse ionized gas), the warm and cold neutral medium (WNM, CNM), photon-dominated regions (or photodissociation regions; PDRs (Hollenbach & Tielens 1999)) and the edges of molecular clouds[3] (Pineda et al. 2013) all contribute to the total [CII] luminosity. We discuss the relative contribution of these phases to the total [CII] luminosity in the context of high redshift galaxies below.

[3] In particular those regions where neutral hydrogen (HI) has already been transformed into H_2 (protected by self-shielding), but the column densities are low enough for that C^+ has not yet transitioned to C^0 and CO (e.g. Madden 2000; Langer et al. 2010) (also referred to as CO-dark H_2 gas (Pineda et al. 2013)).

For the [CII] luminosity originating in the WNM and CNM, the CNM dominates (>95%) due to the low density of the WNM (Wolfire et al. 2010; Vallini et al. 2013). Large-scale Herschel surveys have found that for the Milky Way, the contribution of the CNM to the total [CII] luminosity is about 21% (Pineda et al. 2013), however this contribution is expected to be substantially lower in high redshift galaxies ($z > 4.5$) due to the increasing temperature of the CMB background. When CMB temperature becomes similar to the spin temperature of [CII] in the CNM, the [CII] emission from the CNM is attenuated by >80-90% (Vallini et al. 2013; Lagache et al. 2018). It is thus expected that the CNM and WNM only contribute a negligible amount to the total [CII] luminosity of high redshift galaxies.

In the Milky Way it has been found that the ionized component contributes only 4% to the total [CII] luminosity (Pineda et al. 2013), however, studies of a broader sample of local galaxies have found average contributions of $\sim 20 - 30\%$ (Parkin et al. 2013; Hughes et al. 2017; Díaz-Santos et al. 2017; Croxall et al. 2017; Cormier et al. 2015, 2019). Studies at higher redshifts give similar results (e.g. Stacey et al. 2010; Decarli et al. 2014; Gullberg et al. 2015). This is corroborated by simulations of high redshift galaxies, which also find that ionized gas can contribute around $\sim 20-40\%$ to the total [CII] luminosity (Accurso et al. 2016; Olsen et al. 2017). Currently observational constraints at $z > 5$ are unfortunately nonexistent, so it cannot be ruled out that a substantial fraction of the total [CII] luminosity of high redshift galaxies originates from ionized regions. However, it is probably quite low. In particular, studies of local galaxies found that the fraction coming from ionized regions in local (U)LIRGs anti-correlates with dust temperature (Díaz-Santos et al. 2017). In local dwarf galaxies, it was found that the contribution from ionized regions is lower at lower metallicities and higher ionization parameters (Cormier et al. 2019), something that has also been corroborated in simulations (e.g. Lupi & Bovino 2020). Hotter dust temperatures, lower metallicities and higher ionization parameters are precisely the conditions we expect in high-redshift galaxies (e.g. Stark et al. 2016; J. Bouwens et al. 2016; Sommovigo et al. 2020). It is therefore likely that the contribution from ionized regions to the total [CII] luminosity in high redshift galaxies most likely is quite limited (<10%). However, more observations are essential to properly constrain this, for example using the $[NII]_{122\mu m}$ and/or $[NII]_{205\mu m}$ lines (Oberst et al. 2006; Hughes et al. 2017).

This means that most likely the majority of [CII] emission (>60%−90%) in high redshift galaxies originates from PDRs and the edges of molecular clouds. This is already the case in the Milky Way, where ∼75% of the total [CII] luminosity originates from these regions: ∼47% originates from dense PDR regions and ∼28% from CO-dark H_2 clouds (Pineda et al. 2013), consistent with observations in a broad range of local galaxies (Díaz-Santos et al. 2017; Croxall et al. 2017; Parkin et al. 2013; Hughes et al. 2017; Cormier et al. 2015, 2019). This is also seen in simulations of high redshift galaxies, for which the majority of [CII] emission comes from the PDR and molecular phases (Accurso et al. 2016; Olsen et al. 2017; Pallottini et al. 2019). Hence, modeling the physical processes in PDR regions is essential to understanding the origin of [CII] (Ferrara et al. 2019).

1.3.2.2 *Primary physical processes influencing [CII] from PDR regions*

The luminosity of the [CII] line from PDR regions is subject to a complex interplay of physical effects. Below we give a brief review of the parameters which are most often discussed in the literature in the context of high-z galaxies.

One of the primary parameters often used to explain a possible evolution in the luminosity of [CII] compared to the ongoing star formation, is the metallicity. Carbon abundance scales linearly with metallicity and subsequently does the [CII] luminosity at a fixed (hydrogen) column density ($L \propto Z$). Lower metallicities would thus result in lower [CII] luminosities. However, if the total column density is large and shielding is dominated by dust (and assuming a fixed dust-to-metal ratio), the PDR column density scales inversely proportional to the metallicity ($L \propto 1/Z$). In that case, both effects cancel each other and the [CII] luminosity is independent of metallicity ($L \propto Z \times 1/Z \propto constant$) (Pallottini et al. 2019; Ferrara et al. 2019; Harikane et al. 2020). Whether this is the case for high redshift galaxies depends on their metallicity and the total gas column densities of their PDR regions. For lower metallicities, the column densities will need to be increasingly large to compensate for the decreasing carbon abundance. This only works until the dust opacity at the total column density becomes smaller than unity ($\tau_{dust} < 1$) and PDR becomes density bounded, after this point you run out of gas before running out of photons and [CII] becomes sensitive to metallicity (e.g. Vallini et al. 2015; Olsen et al. 2017; Lagache et al. 2018; Pallottini et al. 2019; Ferrara et al. 2019).

A lower dust-to-metals ratio (at fixed metallicity) can also impact the [CII] emission. In most cases, the outer boundary of PDR regions is primarily determined by the dust opacity. Decreasing the dust-to-metals ratio increases the size of PDR regions, which in turn increases the [CII] luminosity. It has been found that the dust-to-metals ratio decreases for lower metallicities (e.g. De Cia et al. 2016; Wiseman et al. 2017; De Vis et al. 2019), possibly due to more efficient dust destruction in those conditions (e.g. Triani et al. 2020). The same reasoning applies to a lower dust-to-gas ratio at fixed metallicities. Lower dust-to-metal or dust-to-gas ratios can increase the [CII] emission from high redshift galaxies.

The ionization parameter can also have a large impact on the [CII] luminosity. Increasing the ionization parameter increases the size of HII regions, but does not impact the outer boundary of the PDR regions, since that is determined by the dust opacity. For a gas cloud or galaxy with a total fixed column density, this effectively shrinks the size of the PDR region and this consequently decreases the [CII] luminosity (e.g. Ferrara et al. 2019). One of the main drivers of a higher ionization parameter is bursty star formation, which is abundant in the early universe (e.g. Stark et al. 2016).

Geometric effects can also impact the [CII] emission. Normally, models often assume that the complete HII region is surrounded by a PDR region (and ultimately embedded in a molecular cloud), but this is not necessarily the case in actual galaxies. One way to model the effects of a more complex geometry is through the PDR coverage factor. A low PDR coverage factor could, for example, be caused by outflows that blow away neutral gas or when the HII regions are primarily density bounded, in particular when the whole galaxy becomes ionized. Decreasing the PDR coverage factor can drastically lower the [CII] emission of high redshift galaxies (e.g. Cormier et al. 2019; Harikane et al. 2020).

Particle density is another parameter that impacts [CII] luminosities. Increasing the density at a fixed ionizing photon flux decreases the ionization parameter, which increases the [CII] luminosity. However, it also changes the size of HII regions and the outer boundary of PDR regions at different rates. In addition, collisional de-excitation also starts playing a role when the density approaches the critical density ($n_e = 3000cm^{-3}$ for H^0 at 100K (Goldsmith et al. 2012)). Finally, carbon chemistry is also important as carbon is stored away in CO with increasing efficiency at higher densities (e.g. Popping et al. 2019). Harikane et al. (2020) modeled these effects for ionization-bounded PDR regions using CLOUDY and found that increasing the density results in lower [CII] luminosities. This is consistent with other studies (e.g. Popping et al. 2019), which also find that increasing the external ISM pressure surrounding molecular clouds (which increases their density) decreases the [CII] emission.

Finally, the CMB background can also have a significant effect on some regions that emit [CII], like the CNM as discussed above. However, for regions with $T > 100K$ and $n_e \gtrsim 100$, where we expect the majority of the [CII] emission to originate, the CMB effects are negligible (e.g. Pallottini et al. 2019; Laporte et al. 2019). Lastly, more exotic effects like thermal saturation of the upper quantum level, grain charging, and X-ray ionization from AGN activity might play an important role in more extreme conditions (e.g. Smith & Edge 2017; Rybak et al. 2019).

1.3.3 *The [OIII]88μm and [OIII]5007Å lines*

In contrast to singly ionized carbon (C+; [CII]), doubly ionized oxygen (O++; [OIII]) requires a significantly higher energy of 35.1 eV to form from O+, an energy level substantially greater than the 13.6 eV needed to ionize hydrogen. Consequently, [OIII] emission is exclusively produced in the ionized phases of the ISM. These phases primarily consist of dense HII regions surrounding young, massive star clusters and the more diffuse Warm Ionized Medium (WIM). However, the contribution from the WIM to the total [OIII] luminosity is generally considered negligible. This is due to the WIM's very low density compared to HII regions and the scarcity of photons with sufficient energy to doubly ionize oxygen far from their stellar sources. Therefore, both the rest-frame optical [OIII]5007Å nebular line and the far-infrared [OIII]88μm fine-structure line are generally accepted to originate almost entirely from the dense, ionized gas within HII regions (e.g. Tielens 2005).

The luminosity of the [OIII] lines is governed by the physical conditions within these HII regions. On a fundamental level, the strength of oxygen emission lines is tied to the abundance of oxygen. For a given ionizing radiation field, a higher gas-phase metallicity provides more oxygen atoms available for ionization, thus leading to potentially more luminous [OIII] emission. The detection of a bright oxygen line in galaxies at cosmic dawn can therefore indicate that rapid chemical enrichment has already occurred in the early universe.

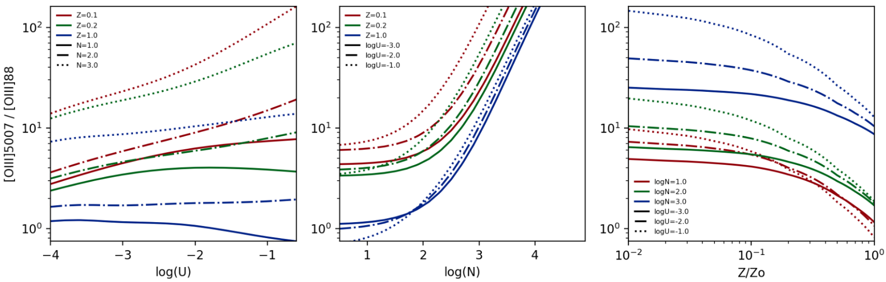

Figure 1.4. The dependence of the [OIII]5007Å/[OIII]88μm line ratio on the dominant ISM properties from Cloudy modelling, ionization parameter (log(U)), density (log(N)) and metallicity ($Z/Z_{\odot}$). The line ratio is most sensitive to the density, as visible from the center panel. The metallicity also has some impact, due to its impact on electron temperature. (Figure is based on CLOUDY models from Witstok et al. 2023.)

Due to its high energy requirement, the production of O++ is also sensitive to the ionization parameter (U), as well as the hardness of the incident radiation field. Environments with high ionization parameters and hard ionizing spectra, typically produced by very young (<10 Myr), massive stellar populations, create larger zones of doubly ionized oxygen, thereby boosting [OIII] emission.

Finally, the density also impacts the line emission of O++; specifically the strength of the [OIII]88μm is suppressed compared to [OIII]5007Å at higher densities. This makes the [OIII]5007Å/[OIII]88μm line ratio a uniquely useful diagnostic of electron density (e.g. Fujimoto et al. 2024).

1.3.3.1 *The [OIII]5007Å/[OIII]88µm Line Ratio*

The ratio of the [OIII]5007Å and [OIII]88µm emission lines serves as a powerful diagnostic of the physical conditions within HII regions, primarily due to their significantly different critical densities for collisional de-excitation. The far-infrared 88µm fine-structure line has a critical density of approximately 500 cm^{-3}, whereas that of the optical 5007Å nebular line is much higher, around 7×10^5 cm^{-3}. Below its critical density, a line's emissivity scales with the square of the electron density (n^2), as nearly every collision leads to a radiative decay. Above the critical density, however, collisional de-excitations become dominant, and the emissivity scales only linearly with density (n) (e.g. Tielens 2005). Consequently, in the density regime between these two values ($\sim10^2$ - 10^5 cm^{-3}), the 5007Å emission grows more rapidly with increasing density than the 88μm emission. This makes their ratio a sensitive probe of the electron density, as illustrated in the central panel of Figure 1.4.

As is also evident from the figure, the line ratio exhibits secondary dependencies on both the gas-phase metallicity and the ionization parameter. Both of these are a consequence of the ratio's dependence on electron temperature (T_e) within the HII regions. A lower metallicity gas contains fewer heavy elements, which are the primary coolants in ionized gas. This results in less efficient cooling and therefore higher equilibrium electron temperatures. Similarly, a higher ionization parameter is also associated with elevated electron temperatures.

This impacts the resulting line ratio because the collisional excitation of the upper energy level for the 5007Å transition requires significantly more energy (2.5 eV) than that of the 88μm transition (0.016 eV). Consequently, the emissivity of the 5007Å is much more sensitive to the electron temperature than the 88μm line. In hotter, lower-metallicity environments, the [OIII]5007Å line is preferentially enhanced relative to the [OIII]88μm line, resulting in a higher overall line ratio.

1.3.4 *Dust Continuum*

Beyond the gaseous components, dust is a crucial ingredient of the ISM. Dust consists of solid, often sub-micron sized particles, primarily composed of heavy elements (metals) such as silicates and carbon, which can condense in various environments. Dust grains are highly effective at absorbing short-wavelength ultraviolet (UV) and optical radiation, which is subsequently re-radiated as thermal emission at longer, far-infrared (FIR) wavelengths. This process of absorption and re-emission significantly impacts what we observe in different parts of the spectrum. On one hand, it means that dust obscures star formation at rest-frame UV and optical wavelengths, necessitating corrections to derive the total star formation rate. On the other hand, the thermal FIR emission provides a direct tracer of this obscured star formation, offering a complementary window into the star-forming activity of galaxies.

Dust is not merely a passive screen, however; it plays an active role in governing the physical processes within the ISM. The surfaces of dust grains act as crucial catalysts for the formation of molecular hydrogen (H_2), the primary fuel for star formation, a process that is otherwise highly inefficient in the gas phase. Furthermore, dust can be an important coolant in dense gas, aiding in the fragmentation of molecular clouds and thereby directly influencing the formation of stars. Perhaps its most critical role in the context of FIR diagnostics is in heating the neutral ISM. Far-ultraviolet (FUV) photons (between 6.0 and 13.6 eV) can strike dust grains and eject energetic electrons via the photoelectric effect. These photoelectrons then heat the surrounding neutral gas through collisions. This heating mechanism is the primary energy source for photodissociation regions (PDRs) and is essential for powering the strong far-infrared cooling lines, especially the [CII] 158μm line (e.g. Tielens 2005).

The production of dust is governed by a few key formation channels. The primary stellar sources are broadly divided into two categories, operating on vastly different timescales. The first, and most rapid, channel is through core-collapse supernovae (SNe). These explosions mark the end of the lives of massive, short-lived stars, injecting newly synthesized dust into the ISM on timescales of just a few tens of millions of years. Given the short timescales involved, SNe are expected to be the dominant dust production mechanism in the early universe (e.g. Michałowski 2015). However, the net dust yield from SNe is still a subject of significant debate, as a substantial fraction of the newly formed grains could be destroyed by the supernova's own reverse shock as it propagates through the surrounding medium.

The second stellar channel involves the stellar winds of asymptotic giant branch (AGB) stars. These are lower-mass, longer-lived stars that enrich the ISM on much longer timescales, typically hundreds of millions of years or more. Consequently, while AGB stars are a major source of dust in the local universe, they are not expected to be a significant contributor to the dust budget of galaxies at the high redshifts explored in this thesis, because at those high redshifts the universe is sufficiently young that not enough time has passed for AGB stars to be a major contributor to the dust budget (e.g. Michałowski 2015).

Finally, in addition to direct stellar production, dust mass can also increase through grain growth within the interstellar medium itself. This process, which involves the accretion of gas-phase metals onto the surfaces of pre-existing 'seed' grains, can operate on either short or very long timescales depending on the local ISM conditions (e.g. Dayal & Ferrara 2018). It could potentially be an important channel for dust mass buildup in the dense, metal-enriched environments of early star-forming galaxies.

A complete understanding of the cosmic dust budget requires considering not only these formation sources but also the processes that remove or destroy dust. Grains can be shattered or sputtered by energetic supernova shocks propagating through the ISM, or they can be permanently removed from a galaxy via powerful galactic outflows. The net amount of dust observed in any galaxy is therefore a complex balance between these sources and sinks, a balance that is crucial for interpreting the properties of high-redshift galaxies.

1.3.5 *Observing the ISM with ALMA and JWST*

The previous sections highlighted how studying the dust continuum emission and emission lines, either in the FIR or UV/optical, is invaluable to gain insight into the properties of galaxies. To study this emission in practice, only a few facilities are sensitive enough and have the wavelength coverage to detect these faint features from distant galaxies.

For the FIR, the Atacama Large Millimeter/submillimeter Array (ALMA) is the most capable instrument, being able to detect the [CII] line in less than an hour in bright z$\sim$7 galaxies and [OIII] in a few hours in the brightest z$\sim$14 galaxy. It should be noted, however, that detecting the dust continuum is generally more difficult than detecting emission lines.

For rest-frame optical lines, at higher redshifts (z$\gtrsim$6), the atmospheric absorption increasingly becomes a problem. For these lines, observations from space are essential, which have become possible with the launch of the James Webb Space Telescope (JWST). This facility has rapidly become the most important tool to study galaxies in the early universe.

1.4 **THIS THESIS**

The overarching goal of studying galaxies at cosmic dawn and the Epoch of Reionization is to understand how the first dark matter haloes were populated with baryonic matter, how they formed stars, and how they subsequently enriched their interstellar media. Within this broad context, several key open questions continue to drive observational efforts: What fraction of early star formation is obscured by dust? How do we robustly identify and characterize galaxies in an increasingly neutral universe? And what are the specific physical conditions—such as ionization state, chemical abundance, and feedback efficiency—within the first generation of galaxies? While a single thesis cannot resolve these fundamental questions, the work presented here provides pieces to this puzzle by leveraging the unique capabilities of ALMA.

Chapter 2 of this thesis addresses the first of these challenges, focusing on early dust buildup and obscured star formation. We utilized the dust continuum to uncover the star formation activity hidden from rest-frame UV view. We targeted a sample of 15 luminous Lyman-break galaxies at z∼7-8 with sensitive ALMA continuum observations, detecting dust emission in six sources and effectively doubling the number of known dust-detected galaxies at z>6.5 at the time. By combining these measurements with deep optical photometry, we constrained the relationship between infrared excess and the UV-continuum slope (IRX–β), finding that these early systems favor a steeper attenuation curve consistent with rapid dust production mechanisms such as supernovae; we also explore the impact of the assumed dust temperature on this result. Crucially, these results demonstrated that even among UV-selected populations, approximately one-third of the star formation is obscured by dust, necessitating significant corrections to the cosmic star formation rate density during the Epoch of Reionization.

Chapter 3 is focused on confirming and characterizing galaxies in the Epoch of Reionization. Before JWST was available, one of the critical bottlenecks in studying high-redshift galaxies was the sheer difficulty of obtaining spectroscopic redshifts. This was made difficult by the lack of strong lines available to ground-based spectroscopy, which at z>6.5 is mostly limited to Lyman-α. Unfortunately, the increasingly neutral universe at these redshifts strongly absorbs this line. Despite its relatively small instantaneous redshift coverage, especially compared to optical spectroscopy, we demonstrate the efficacy of blindly searching for redshifts with ALMA by stitching together multiple observations. Building on the work of Smit et al. (2018), we targeted a sample of six luminous Lyman-break galaxies at z∼7, selected from the COSMOS/UltraVISTA field based on tight photometric redshift constraints derived from Spitzer/IRAC colors. By scanning for the [CII] 158μm line, we achieved reliable detections for 50% of the sample, confirming that this method was highly efficient for UV-bright sources. Beyond providing precise redshifts, these observations enabled a characterization of the ISM and kinematics of these early systems, revealing a surprisingly diverse mix of dynamical states ranging from ordered rotation to complex mergers. These findings confirmed that the [CII] properties of z∼7 galaxies are largely consistent with local scaling relations and validated the observational strategy that laid the groundwork for the REBELS Large Program.

The launch of JWST has spectacularly shifted the observational frontier to the cosmic dawn (z>10), allowing us to directly probe the physical conditions of the very first galaxies. *Chapter 4* presents the ALMA detection of [OIII] 88μm in JADES-GS-z14-0. This observation yields a robust spectroscopic redshift of z=14.179, making it the most distant confirmation achieved with ALMA to date. The detection reveals a surprisingly chemically enriched system (Z$\sim$0.1-0.2 $Z_\odot$) just 300 million years after the Big Bang, while the non-detection of the dust continuum places strict constraints on early dust production mechanisms. These results demonstrate that even in the JWST era, ALMA remains an indispensable tool for characterizing the physical state and rapid evolution of the earliest known galaxies.

Finally, addressing the open question of how feedback regulates early galaxy formation, *Chapter 5* delves deeper into the physical state of this primordial galaxy through deep ALMA observations targeting the [CII] 158μm line. In contrast to the bright [OIII] emission, [CII] remained undetected, placing a lower limit on the [OIII]/[CII] ratio (>3.5) consistent with an interstellar medium characterized by extreme ionization conditions and surprisingly low gas densities. By using the [CII] limit as a tracer for the neutral gas reservoir, we inferred a relatively low gas fraction (f_{gas} <0.77), which stands in contrast to the gas-rich nature expected at these redshifts. When combined with the absence of dust continuum, these results suggest that strong feedback from a recent starburst may have efficiently expelled much of the fuel from the galaxy, painting a picture of JADES-GS-z14-0 as a rapidly evolving system caught in a violent "post-outflow" phase.

REFERENCES

Accurso, G., Saintonge, A., Bisbas, T. G., & Viti, S. 2016, Monthly Notices of the Royal Astronomical Society, 464, 3315–3330.

Benson, A., Bower, R., Frenk, C., et al. 2003, The Astrophysical Journal, 599, 38–49.

Carniani, S., Hainline, K., D'Eugenio, F., et al. 2024, Nature, 633, 318

Cormier, D., Madden, S. C., Lebouteiller, V., et al. 2015, Astronomy & Astrophysics, 578, A53.

Cormier, D., Abel, N. P., Hony, S., et al. 2019, Astronomy & Astrophysics, 626, A23.

Croxall, K. V., Smith, J. D., Pellegrini, E., et al. 2017, The Astrophysical Journal, 845, 96.

Dayal, P., & Ferrara, A. 2018, PhR, 780, 1

De Cia, A., Ledoux, C., Mattsson, L., et al. 2016, Astronomy amp; Astrophysics, 596, A97.

De Vis, P., Jones, A., Viaene, S., et al. 2019, Astronomy amp; Astrophysics, 623, A5.

Decarli, R., Walter, F., Carilli, C., et al. 2014, The Astrophysical Journal, 782, L17.

Dekel, A., Birnboim, Y., Engel, G., et al. 2009, Nature, 457, 451

Díaz-Santos, T., Armus, L., Charmandaris, V., et al. 2017, The Astrophysical Journal, 846, 32.

Ferrara, A., Vallini, L., Pallottini, A., et al. 2019, Monthly Notices of the Royal Astronomical Society, 489, 1–12.

Fujimoto, S., Ouchi, M., Nakajima, K., et al. 2024, The Astrophysical Journal, 964, 146.

Goldsmith, P. F., Langer, W. D., Pineda, J. L., & Velusamy, T. 2012, The Astrophysical Journal Supplement Series, 203, 13.

Gullberg, B., De Breuck, C., Vieira, J. D., et al. 2015, Monthly Notices of the Royal Astronomical Society, 449, 2883–2900.

Gunn, J. E., & Gott, III, J. R. 1972, ApJ, 176, 1

Harikane, Y., Ouchi, M., Inoue, A. K., et al. 2020, The Astrophysical Journal, 896, 93.

Harikane, Y., Ouchi, M., Oguri, M., et al. 2023, ApJS, 265, 5

Hollenbach, D., & Tielens, A. 1999, Reviews of Modern Physics, 71, 173

Hughes, T. M., Ibar, E., Villanueva, V., et al. 2017, Astronomy & Astrophysics, 602, A49.

J. Bouwens, R., Aravena, M., Decarli, R., et al. 2016, The Astrophysical Journal, 833, 72.

Lagache, G., Cousin, M., & Chatzikos, M. 2018, Astronomy & Astrophysics, 609, A130.

Langer, W. D., Velusamy, T., Pineda, J. L., et al. 2010, Astronomy and Astrophysics, 521, L17.

Laporte, N., Katz, H., Ellis, R. S., et al. 2019, Monthly Notices of the Royal Astronomical Society: Letters, 487, L81–L85.

Lupi, A., & Bovino, S. 2020, Monthly Notices of the Royal Astronomical Society, 492, 2818–2827.

Madden, S. C. 2000, New Astronomy Reviews, 44, 249–256.

Michałowski, M. J. 2015, Astronomy amp; Astrophysics, 577, A80.

Mo, H., van den Bosch, F. C., & White, S. 2010, Galaxy Formation and Evolution, doi:10.1017/CBO9780511807244

Moster, B. P., Naab, T., & White, S. D. M. 2013, MNRAS, 428, 3121

Oberst, T. E., Parshley, S. C., Stacey, G. J., et al. 2006, The Astrophysical Journal, 652, L125–L128.

Olsen, K., Greve, T. R., Narayanan, D., et al. 2017, The Astrophysical Journal, 846, 105.

Pallottini, A., Ferrara, A., Decataldo, D., et al. 2019, Monthly Notices of the Royal Astronomical Society, 487, 1689–1708.

Parkin, T. J., Wilson, C. D., Schirm, M. R. P., et al. 2013, The Astrophysical Journal, 776, 65.

Pineda, J. L., Langer, W. D., Velusamy, T., & Goldsmith, P. F. 2013, Astronomy & Astrophysics, 554, A103.

Planck Collaboration, Akrami, Y., Ashdown, M., Aumont, J., et al. 2020, Astronomy amp; Astrophysics, 641, A11.

Popping, G., Pillepich, A., Somerville, R. S., et al. 2019, The Astrophysical Journal, 882, 137.

Press, W. H., & Schechter, P. 1974, ApJ, 187, 425

Revaz, Y., Jablonka, P., Sawala, T., et al. 2009, A&A, 501, 189

Rybak, M., Rivera, G. C., Hodge, J. A., et al. 2019, The Astrophysical Journal, 876, 112.

Schaye, J., Crain, R. A., Bower, R. G., et al. 2015, Monthly Notices of the Royal Astronomical Society, 446, 521

Smit, R., Bouwens, R. J., Carniani, S., et al. 2018, Nature, 553, 178

Smith, R. J., & Edge, A. C. 2017, Monthly Notices of the Royal Astronomical Society: Letters, 471, L66–L70.

Sommovigo, L., Ferrara, A., Pallottini, A., et al. 2020, Monthly Notices of the Royal Astronomical Society, 497, 956–968.

Stacey, G. J., Hailey-Dunsheath, S., Ferkinhoff, C., et al. 2010, The Astrophysical Journal, 724, 957–974.

Stark, D. P., Ellis, R. S., Charlot, S., et al. 2016, Monthly Notices of the Royal Astronomical Society, 464, 469–479.

Tielens, A. G. G. M. 2005, The Physics and Chemistry of the Interstellar Medium

Triani, D. P., Sinha, M., Croton, D. J., Pacifici, C., & Dwek, E. 2020, Monthly Notices of the Royal Astronomical Society, 493, 2490–2505.

Vallini, L., Gallerani, S., Ferrara, A., & Baek, S. 2013, Monthly Notices of the Royal Astronomical Society, 433, 1567.

Vallini, L., Gallerani, S., Ferrara, A., Pallottini, A., & Yue, B. 2015, The Astrophysical Journal, 813, 36.

Vogelsberger, M., Genel, S., Springel, V., et al. 2014, Monthly Notices of the Royal Astronomical Society, 444, 1518

Weibel, A., Oesch, P. A., Barrufet, L., et al. 2024, Monthly Notices of the Royal Astronomical Society, 533, 1808.

Wiseman, P., Schady, P., Bolmer, J., et al. 2017, Astronomy amp; Astrophysics, 599, A24.

Witstok, J., Jones, G. C., Maiolino, R., Smit, R., & Schneider, R. 2023, Monthly Notices of the Royal Astronomical Society, 523, 3119.

Wolfire, M. G., Hollenbach, D., & McKee, C. F. 2010, The Astrophysical Journal, 716, 1191.